Impaired speed encoding is associated with reduced grid cell periodicity in a mouse model of tauopathy

Thomas Ridler [1], Jonathan Witton [2], Keith G. Phillips [3], Andrew D. Randall [1], Jonathan T. Brown* [1]

1. Institute of Biomedical and Clinical Sciences,
   University of Exeter Medical School,
   University of Exeter,
   Hatherly Laboratories,
   Prince of Wales Road,
   Exeter, EX4 4PS, UK

2. School of Physiology, Pharmacology and Neuroscience,
   University of Bristol,
   University Walk,
   Bristol, BS8 1TD, UK

3. Lilly UK
   Erl Wood Manor
   Windlesham,
   Surrey, GU20 6PH, UK

*Corresponding author: Dr Jonathan Brown, Institute of Biomedical and Clinical Sciences, University of Exeter Medical School, College of Medicine and Health, Hatherly Laboratories, Prince of Wales Road, Exeter, EX4 4PS, UK, Tel: +441392725504, Email: J.T.Brown@exeter.ac.uk.

Abstract

Dementia is associated with severe spatial memory deficits which arise from dysfunction in hippocampal and parahippocampal circuits. For spatially-sensitive neurons, such as grid cells, to faithfully represent the environment these circuits require precise encoding of direction and velocity information. Here we have probed the firing rate coding properties of neurons in medial entorhinal cortex (MEC) in a mouse model of tauopathy. We find that grid cell firing patterns are largely absent in rTg4510 mice, while head direction tuning remains largely intact. Conversely, neural representation of running speed information was significantly disturbed, with smaller proportions of MEC cells having firing rates correlated with locomotion in rTg4510 mice. Additionally, the power of local field potential oscillations in the theta and gamma frequency bands, which in wildtype mice are tightly linked to running speed, was invariant in rTg4510 mice. These deficits in locomotor speed encoding likely severely impact path integration systems in dementia.

Introduction

Accurate spatial navigation requires the integration of sensory information to generate neural representations of space. Various high-level representations of the external environment are expressed at a single cell level within the extended hippocampal formation (hippocampus proper, dentate gyrus, entorhinal cortex and subiculum) and connected brain areas, regions well known to be critical for spatial memory. For example, place cells in the hippocampus fire action potentials in specific spatial locations[1], whilst grid cells in the medial entorhinal cortex (MEC) fire in a highly organised, hexagonally distributed spatial pattern across an environment[2,3]. These directly spatially-sensitive neurons are collocated within the MEC with other functionally defined cell types, including head-direction[4–7], speed[8,9] and border cells[10,11]. Together these are thought to provide the crucial computational information required for effective path integration, the process of using idiothetic cues to continuously calculate update positional information[12].

Patients with Alzheimer's disease (AD) and other dementia-spectrum disorders exhibit profound disruption in spatial navigation and memory, even at very early stages of the diseas[13–17]. At a pathological level, misfolded tau deposition typically occurs first in the entorhinal cortex and hippocampus[18]. Taken together, these clinical signs strongly implicate pathology-induced circuit-level dysfunction in the hippocampal formation as a key early-stage functional deficit in AD. In this regard, there is substantial evidence from transgenic mouse models that dementia pathologies, such as β-amyloid deposition (Aβ) and hyperphosphorylation and misfolding of tau can disrupt the intrinsic properties[19–22] and synaptic microcircuits[23–25] of pyramidal cells in CA1 of hippocampus. Furthermore, there is growing evidence that place cells in the CA1 region of APP and tau overexpressing mice have reduced spatial-sensitivity[19,26,27], strongly suggesting a failure of some aspects of the upstream functional circuits involved in spatial cognition. Recent evidence suggests that the circuits required for generation of theta and gamma frequency oscillations in the dorsal entorhinal cortex are especially prone to dysfunction in a mouse model of tauopathy (rTg4510 mice)[28].

Furthermore, Fu *et al.*, (2017) showed that grid cell spatial periodicity is reduced in a mouse in which tau overexpression is restricted to the entorhinal cortex. These data correlate with human imaging studies which suggest deficits in grid cell-like activity in the entorhinal cortices of people at genetic risk of developing AD[30].

Importantly, the effect of tau pathology on other functional components of the spatial navigation system is not known. In this study we report for the first time that disruption to speed encoding in the MEC of rTg4510 mice may underlie deficits in grid cell function. Using high-density silicone probes and tetrode recording approaches in freely moving animals, we report that in both the medial entorhinal cortex and the CA1 region of the hippocampus, encoding of speed information at both the local field potential and cellular level is substantially impaired. We propose a model whereby such deficiencies in speed encoding networks result in loss of grid cell firing patterns in the MEC.

Results

Tau pathology is associated with loss of oscillatory speed coding

Neural coding of spatial information is likely to require the precise representation of locomotor speed[12,31–33]. Velocity information can be represented in the brain via the dynamic regulation of the power and frequency of neuronal network oscillations in the theta and gamma frequency bands[34–38]. We hypothesised that the profound deficits in spatial memory that occur in response to tau pathologies[19,29,39] arise from impaired representation of locomotor speed in the hippocampal formation, ultimately leading to deficits in the encoding of spatial information. To examine this hypothesis we implanted multi-site silicone-based recording probes in the dorsal MEC of male wildtype (WT) and rTg4510 mice (6-7 months). Following a post-surgical recovery period, mice were encouraged to explore a familiar linear track, baited by food rewards at either end to encourage running between the two ends, whilst connected to a multi-channel electrophysiological recording apparatus via a lightweight tether cable.

As expected, in WT mice, theta oscillation properties followed changes to locomotor activity (fig 1A/B). Pooled data illustrate a clear relationship between running speed and theta oscillation power (linear regression: R^2=0.71, p<0.001, n=7 mice) and frequency (linear regression: R^2 = 0.69, p < 0.001, n = 7 mice) (fig 1Ci). In contrast, in rTg4510 mice, theta oscillation amplitude was poorly correlated with locomotor activity and remained at consistent levels throughout recording sessions (linear regression: R^2 = 0.15, p = 0.02, n = 8 mice, fig 1Ci). Importantly the overall Z-transformed correlation coefficient and slope relationships for theta power-running speed relationships were significantly lower in rTg4510 mice when compared to WT controls (2-way repeated measures ANOVA, see Table 1 and Figure 1D). Although less pronounced than in WT animals, peak theta frequency was correlated with running speed in rTg4510 mice (linear regression: R^2 = 0.74, p < 0.01, n = 8 mice, Figure 1Cii) which, across the population was not significantly different from WT (Correlation (Z'); WT: 0.84 ± 0.24, rTg4510: 0.40 ± 0.14, unpaired T-test, p = 0.13, n = 7/8 mice), with no difference in the slope of the frequency-running speed relationship (Correlation (Hz/cms^{-1}'); WT: 0.045 ± 0.0077, rTg4510: 0.037 ± 0.011, unpaired T-test, p = 0.53, n = 7/8 mice) .

Similar running speed modulation has been observed in both in the fast (60-120 Hz) and slow (30-50 Hz) gamma frequency bands[36,37]. In WT mice, both fast and slow gamma oscillation power was positively correlated with running speed (linear regression; fast gamma: R^2 = 0.90, p < 0.001, n = 7 mice; slow gamma: R^2 = 0.17 p = 0.013, n = 8 mice), although the slope of this association was greater for fast gamma frequencies (slow gamma: 27.1 ± 8.4 mV^2/Hz.cm^{-1}, fast gamma: 80.6 ± 19.2 mV^2/Hz.cm^{-1}; 2-way repeated measures ANOVA; Table 1 and Figure 1D). rTg4510 mice did not show significant correlations for fast gamma frequency band oscillations (linear regression; fast gamma: R^2 = 0.03, p = 0.67, n = 8 mice, Figure 1D), but did for slow gamma frequencies (R^2 = 0.43, p < 0.01, n = 8 mice, Figure 1D). However, compared to the WT population, this correlation was significantly lower only in the higher gamma frequency range (2-way repeated measures ANOVA, Table 1 and Figure 1D, n = 7/8 mice).

Loss of grid rhythmicity in rTg4510 mice

Impairments to the theta oscillatory code for running speed may impair grid cell rhythmicity. To establish whether this was the case, we used high density silicone probes to isolate a total of 279 single-units in layer II/III of the dorsal MEC from 10 mice (WT:150 units from 5 mice, rTg4510: 129 units from 5 mice). In this study we focused on the dorsal MEC, a subregion which has previously been identified as being particularly vulnerable in this transgenic model[28]. By performing post-hoc electrolytic lesions on each recording shank to identify probe location, we were able to estimate individual unit location by determining the largest average waveform along the 200 μm probe for each isolated unit. Importantly, estimated recording location was not different between genotypes (Median distance from dorsal entorhinal border (interquartile range (IQR)): WT: 350(350) μm, rTg4510: 385(275) μm, U = 9660, p = 0.77, Mann-Whitney U test; Figure S1A).

Considered across the entire cellular population, MEC single units recorded from rTg4510 mice exhibited a small decrease in mean firing rate (Median (IQR): WT: 2.97 (16.7) Hz, rTg4510: 1.03 (3.0) Hz, U = 4472, p = 0.01, Mann-Whitney U, n = 150; 129 units, Figure S1E). As in the CA1 region of the hippocampus[19], rTg4510 cells also showed a pronounced decrease in theta modulation of firing patterns (Median (IQR) theta modulation index: WT: 9.17 (13.9), rTg4510: 2.29 (2.81), U = 2296, p < 0.001, Mann-Whitney U, n = 150;129 units, Figure S1C). Individual units with a theta modulation index (TMI) greater than 5[40] were assigned as 'theta modulated'. While the majority of WT MEC cells (65%) showed significant theta modulation, only a small proportion (13%) passed threshold in rTg4510 mice (χ^2 (1) = 64.1, p < 0.0001, Chi-Square test, Figure S1D). Extracellularly-recorded spike waveforms from interneurons in the mEC have a significantly narrower spike widths when compared to excitatory neurons[41]. The probability distributions of single units spike widths recorded from the dorsal MEC in WT mice had a bimodal distribution (Figure S1F). Based on this distribution and previously published work[41], we classed units with spike widths <0.35 ms as putative interneurons and those >0.35 ms as putative excitatory cells. Using this approach we found

that 47/150 units (31%) were classed as putative interneurons in WT mice, where as in rTg4510 mice a significantly smaller proportion of units were classed as putative interneurons (8/129 units, 15%; χ^2 (1) = 16.0, p < 0.001, Chi-Square test; Figure S1G).

Consistent with the literature we found that ~1/4 of cells in the WT MEC had grid-like spatial firing patterns in a 0.8 m x 0.8 m square arena. We calculated a grid score for each cell, based on the rotational symmetry of the 2D-autocorrelations and found that 36/150 cells (24%) had grid scores higher than the 95th percentile of the distribution produced from shuffled spike timestamps (threshold = 0.21; Figure 2B). In contrast, in rTg4510 mice there was an almost complete breakdown of grid cell periodicity (3/129 units, 2.3%, threshold: 0.26), with animals displaying irregular, non-uniform, firing fields across recording environments (χ^2 (1) = 27.1, p < 0.0001, Chi-Square test, Figure 2A/C). Furthermore, the distribution of grid scores of all cells recorded from WT and rTg4510 mice was significantly different (Median (IQR) grid score: WT, 0.03 (0.3); rTg4510, 0 (0.12), n = 150/129 units; P < 0.001; Mann-Whitney U).

Conversely, when measuring the spatial information content (SI) of recorded cells[42], we found that MEC neurons did not differ significantly between genotypes, either as a distribution (WT, -0.05 (0.71), n = 150; rTg4510, 0 (0.24), n = 129 units; P > 0.05; Mann-Whitney U) or in the proportion of cells that exceed threshold (WT: 10/150, rTg4510 6/129, χ^2 (1) = 0.52, p = 0.47 Chi-Square test; data not shown).

Tau pathology is associated with impaired speed coding in MEC single units

Deficits in running speed-oscillation relationships at a local field potential level suggest alterations in the neural representation of running speed in the MEC of rTg4510 mice. Recent evidence suggests the existence of a separate population of cells in the MEC which express a rate code for running speed ('speed cell')[8]. We calculated a speed score for all recorded cells, whilst mice ran on an L-shaped track, by computing the Fisher-transformed correlation coefficient (z) between instantaneous firing frequency and running speed (Figure 3A-B). Units

were considered 'speed-modulated' if they had a speed score outside the 5-95 centile range of a shuffled distribution of data produced from 250 shuffles for each cell (Figure 3C). In WT mice, 85/150 (57 %) cells had firing rates significantly modulated by running speed, whereas in rTg4510 mice a significantly lower proportion of cells was speed modulated (17/129; 13%; χ^2 (1) = 56.55, $p < 0.0001$, Chi-Square test, Figure 3E). As an overall population, rTg4510 MEC units also displayed a significantly lower average speed score compared to WT mice (Median (IQR): WT: z = 0.11(0.31), rTg4510: z = 0.009(0.01), U = 3603, $p < 0.0001$, Mann-Whitney U, n = 150;129 units, Figure 3D), with cells recorded from rTg4510 mice, on average displaying a running speed correlation close to zero.

Speed modulated MEC neurons can be broadly split into those that display linear and saturating exponential relationships between running speed and firing rate[9]. To account for this, speed scores were calculated for log transformed data and further classified as linear or exponential by the best regression fit (Figure S2A). In WT animals speed-modulated cells showed an approximately equal distribution between linear and saturating running speed relationships (Figure S2B linear: 41/85 units, saturating: 44/85 units, which did not differ significantly in the remaining rTg4510 MEC neurons (linear: 10/17 units, saturating: 7/17 units, χ^2 (1) = 0.6, p = 0.43 Chi-Square test, Figure S2B).

Previous studies have suggested that a small proportion of speed-modulated cells decreased their firing frequency during locomotor activity[8,9]. On the linear track, in WT mice, this population was observed to be consistent with previous reports (~13% of speed modulated cells)[8,9]. In contrast, in rTg4510 mice the proportion of cells with negative speed relationships was substantially and significantly higher (WT: 11/85 units, rTg4510: 7/17 units, χ^2 (1) = 7.8, p = 0.005, Chi-Square test, Figure S2C), meaning that speed modulated cells were split much more evenly between positive and negative associations with firing rate. Given that many MEC speed cells are fast spiking in nature[8], we also assessed the spiking properties the recorded of speed-sensitive units. We found that in WT and rTg4510 mice, a similar proportion (41%

and 31%, respectively; χ^2 (1) = 0.6, p = 0.4, Chi-Square test) of speed-modulated neurons were fast-spiking (mean firing rate >10 Hz) (Figure S2E). The proportion of all cells that were classified as fast-spiking was substantially lower in rTg4510 mice (13% vs 30% in WT; χ^2 (1) = 19.0, p <0.001, Chi-Square test; Figure S2E), although this likely reflects the overall reduction in mean firing rate in these neurons (Figure S1E).

Speed modulated firing of single units has also been observed in the hippocampus[8,43,44], so we next sought to determine whether deficits in speed tuning in rTg4510 mice were specific to the MEC, or were also represented downstream in the hippocampus proper. For this purpose, data were taken from previous single unit and local field potential recordings in the hippocampal CA1 region of rTg4510 mice (Booth et al., 2016b) at a similar age point and reanalysed to assess the contribution of locomotor activity to firing rate. In this region, CA1 theta band activity in the local field potential was also correlated with running speed in WT mice (linear regression; theta power; WT: R^2 = 0.83, p < 0.001, n = 6 mice), but not in rTg4510 mice (linear regression: R^2 = -0.04, p = 0.6, n = 4 mice, Figure S3A). A significant proportion of CA1 neurons had firing rates modulated by running speed in both WT and rTg4510 mice (WT: 25/46 units, rTg4510: 27/52 units). Importantly however, as seen in MEC recordings, a much greater proportion of CA1 cells were negatively modulated by locomotor activity in rTg4510 mice than in WT controls (WT: 5/25 units, rTg4510:13/27 units; χ^2 (1) = 4.5, p = 0.03, Chi-Square test, Figure S3F).

Normal head-direction tuning in rTg4510 mice

Another critical component of the path integration system in the MEC are cells which accurately encode directional heading information. Therefore, we next sought to establish whether head direction cells[4,5] in the MEC were similarly disrupted in rTg4510 mice. We calculated a head direction score (HD) by determining the mean vector length of circular firing distributions and, as with other functional metrics, we compared observed HD scores with shuffled distributions (Figure 4A&B). Importantly, a similar proportion of MEC cells in WT and

rTg4510 mice surpassed the 95th-centile threshold (WT: 19/150, rTg4510: 14/129, χ^2 (1) = 0.79, p = 0.37, Chi-Square test, Figure 4C). Furthermore, as a population, the HD score was actually slightly, but significantly, higher in rTg4510 cells compared to WT (Median (IQR) vector length: WT: 0.074(0.091), rTg4510: 0.11(0.12), U = 6509, p = 0.0014, Mann-Whitney U, n = 150;129 units, Figure 4B-E). These data suggest that head-direction tuning remains intact in rTg4510 mice. Similarly, there was no change in the proportion of border cells observed across genotypes (WT: 4/150, rTg4510: 6/129, χ^2 (1) = 0.79, p =0.37, Chi-Square test; data not shown), with relatively small numbers of cells passing threshold produced from shuffled datasets. Neither was there a difference in the average border score between the two populations (Median (IQR) vector length: WT: 0.097(0.67), rTg4510: -0.04(0.78), U = 6191, p = 0.94, Mann-Whitney U, n = 150; 129 units; data not shown).

A proportion of cells within the MEC are known to demonstrate conjunctive functional representation[5]. Using the tuning-curve approaches defined above, we found that ~60% of WT cells passed the threshold for only a single functional class of neuron (i.e. grid-, speed- or HD-cells). A further ~25% of WT cells passed the threshold for more than one functional class and were therefore conjunctive cells, whilst the remaining ~20% of cells were unclassified (Figure S4D). For example, in this study, only 3% of spatially sensitive cells were pure grid cells, whilst the remaining grid cells also passed the threshold for speed- and HD-modulation (Figure S4C). In contrast, due to the substantial reduction in numbers of speed and grid cells, very few rTg4510 cells (~2%) expressed any conjunctive representation (Figure S4D).

230

Correlation (Z)					
Source of Variation	Df	Sum-of-squares	Mean square	F	P
Frequency	2	0.470	0.235	4.341	0.051
Genotype	1	0.602	0.602	5.927	0.038
Interaction	2	1.330	0.665	8.379	0.005
Slope ($mV2/Hz.cm^{-1}$)					
Source of Variation	Df	Sum-of-squares	Mean square	F	P
Frequency	2	0.004	0.002	8.973	0.004
Genotype	1	0.008	0.008	86.224	>0.001
Interaction	2	0.005	0.003	16.623	>0.001

Table 1: Results of 2-Way repeated measure ANOVA for oscillation-running speed interaction. Results of relevant *post-hoc* pairwise-comparisons displayed on Figure 1.

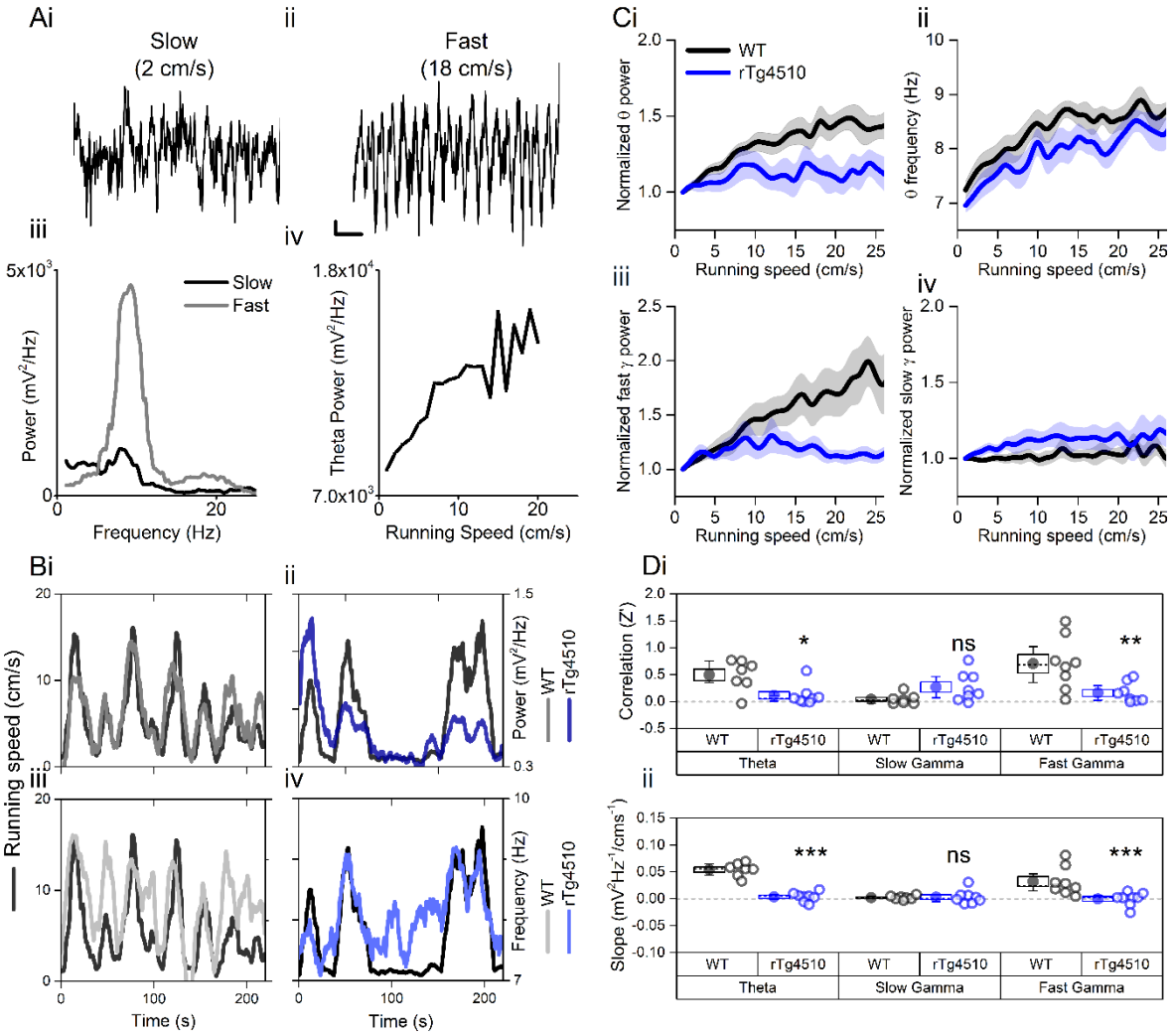

231

Figure 1: Oscillation-running speed relationship is impaired in rTg4510 mice. A) Local field potential from periods of slow (**i**) and fast (**ii**) running speed showing faster and larger theta oscillations during locomotor activity. **iii)** Power spectra of data shown in i and ii for slow (black) and fast (grey) running periods. **iv)** Example relationship between running speed and average theta oscillation power across recording session. **B)** Example plots showing animals running speed on linear track (black, left Y axis) showing high correlation with theta oscillation (grey, right Y axis) power (**i**) and frequency (**iii**) over several minutes of recording. Corresponding example from rTg4510 mouse showing with theta oscillation amplitude (**ii**) and frequency (**iv**) with decreased association with running speed. **C)** Running speed -theta oscillation relationships for power (**i**; normalised to 1-2 cm/s bin) and frequency (**ii**). Also shown are fast (**iii**) and slow (**iv**) gamma power-running speed relationships. **D)** Pooled data for each animal showing Z-transformed correlation coefficients (**i**) and slopes (**ii**) of running speed-oscillatory power relationships for different frequency bands (* $p<0.05$, ** $p<0.01$, *** $p<0.001$, ns = not significant, Bonferroni-corrected pairwise-multiple comparisons; for 2-way repeated measures ANOVA main effects and interactions see Table 1).

232

233

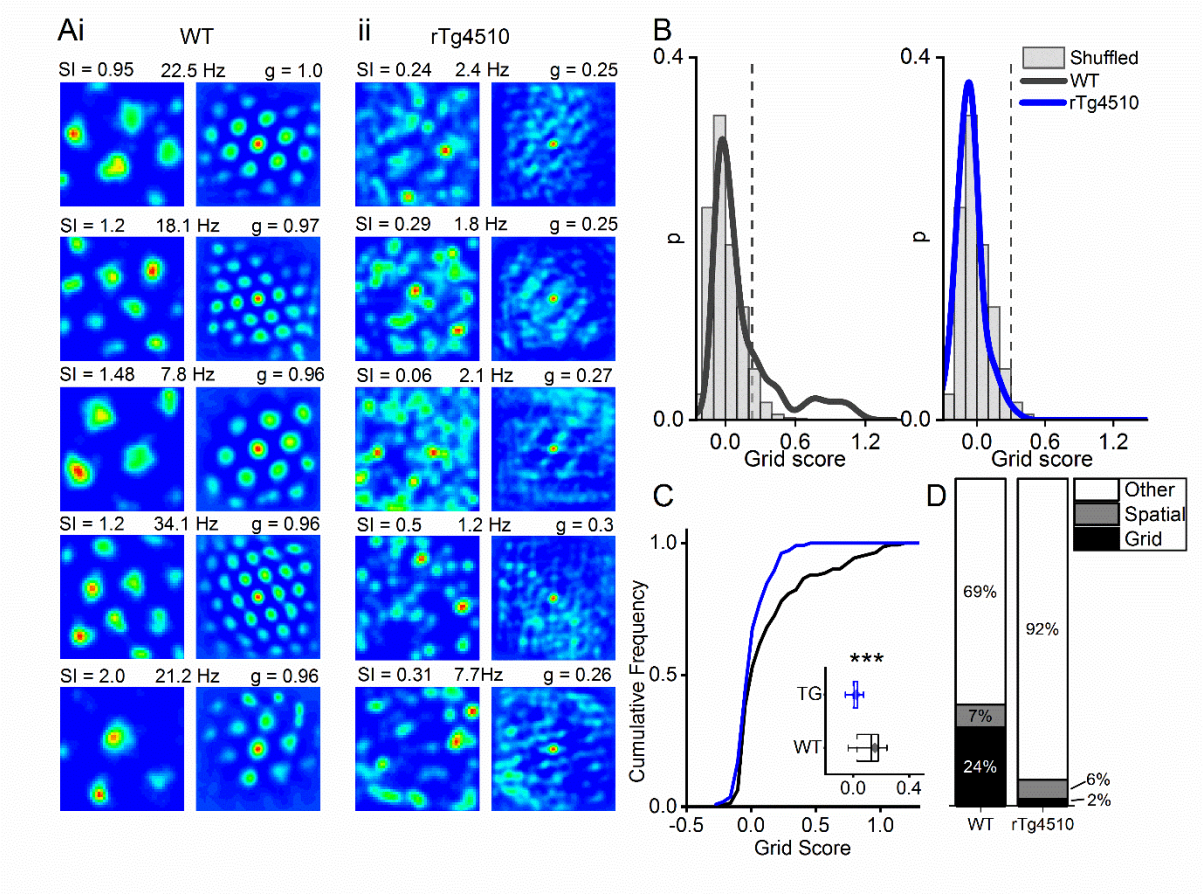

Figure 2: Breakdown of grid cell periodicity in rTg4510 mice. A) Example spatial firing patterns (left) and 2D autocorrelations (right) of cells from WT (**i**) and rTg4510 (**ii**) mice in a 0.8 x 0.8 m square arena, displayed with grid score (g), spatial information content (SI) and peak firing rate across recording environment. 5 cells with the highest grid score displayed for each genotype. **B)** Histograms of grid scores for all single units recorded from WT and rTg4510 mice. Observed data plotted as a solid line, shuffled data shown as grey bars. The 95th centile of shuffled distributions is plotted as a dashed line. **C)** Cumulative frequency plots for grid score; *inset* box plot illustrating average values for each genotype (dotted line: median, diamond: mean ± SEM, whiskers: 25th/75th centile), *** p<0.001, Mann-Whitney U test. **D)** Proportions of grid and spatial non-grid cells greater than threshold in WT and rTg4510 mice.

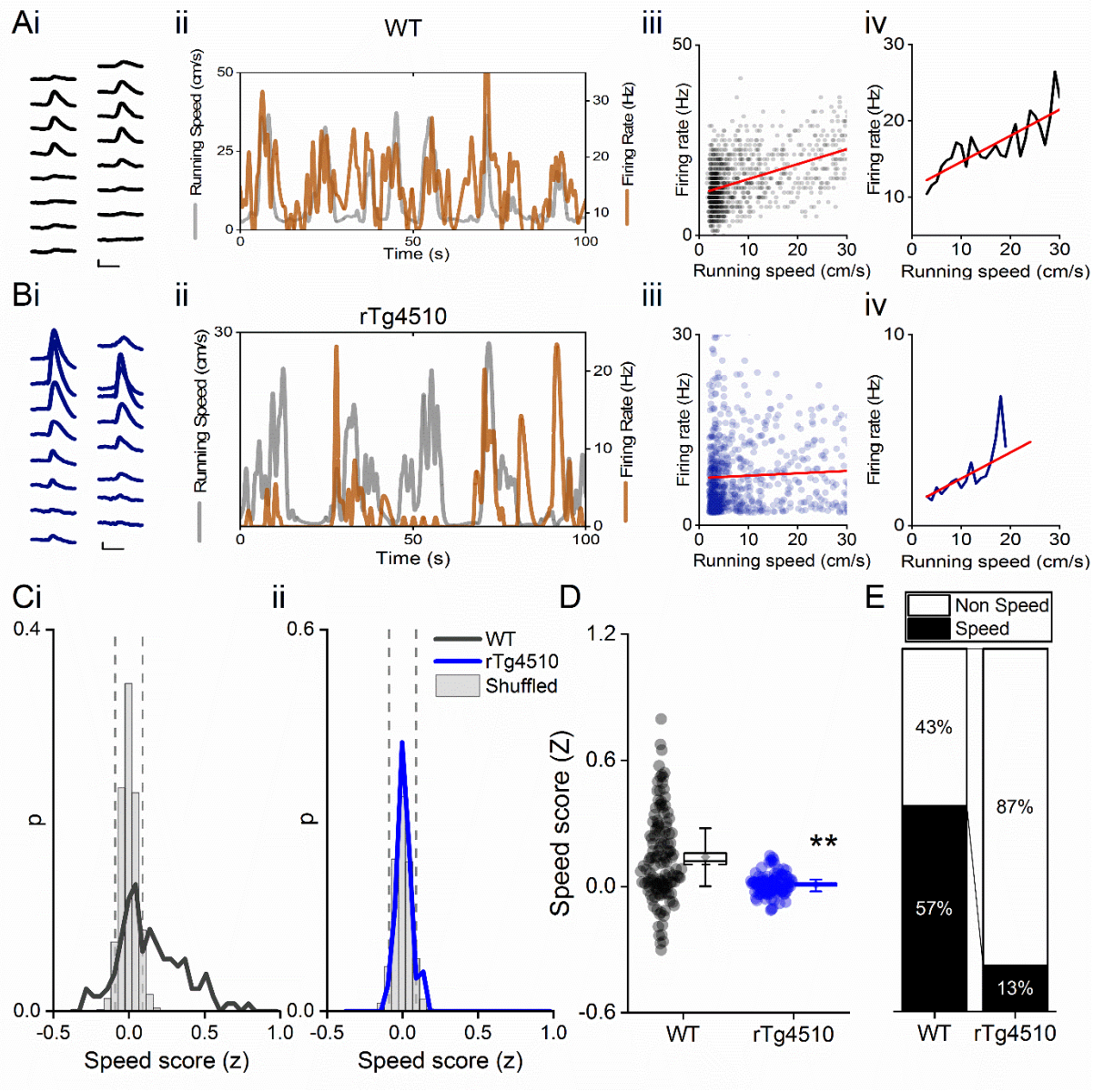

234

Figure 3: Decreased speed modulation of MEC single units in rTg4510 mice. Average waveforms of a single unit recorded from a 16 channel shank silicone probe, from a WT (**Ai**; black) and rTg4510 (**Bi**; blue) mouse. The running speed (grey) and cell firing rate (orange) (**ii**), correlation between running speed and firing rate for each time bin (40 ms) **(iii),** and average for each speed bin (1 cm/s) (**iv**) are shown for each of these example cells. Red line: linear fit for each. Scale bars: 0.3 ms, 25 µV. **C)** Distribution of speed scores for WT (**i**) and rTg4510 units (**ii**) with shuffled distribution of scores (grey bars); 5^{th}/95^{th} centile threshold: dotted lines. **D)** Average speed score for each recorded MEC unit. Box plots: dotted line: median, diamond: mean ± SEM, whiskers: 25^{th}/75^{th} centile), ** p<0.01, Mann-Whitney U test. **E)** Proportion of cells classified as speed modulated (>95^{th} or <5^{th} centile of shuffled distribution).

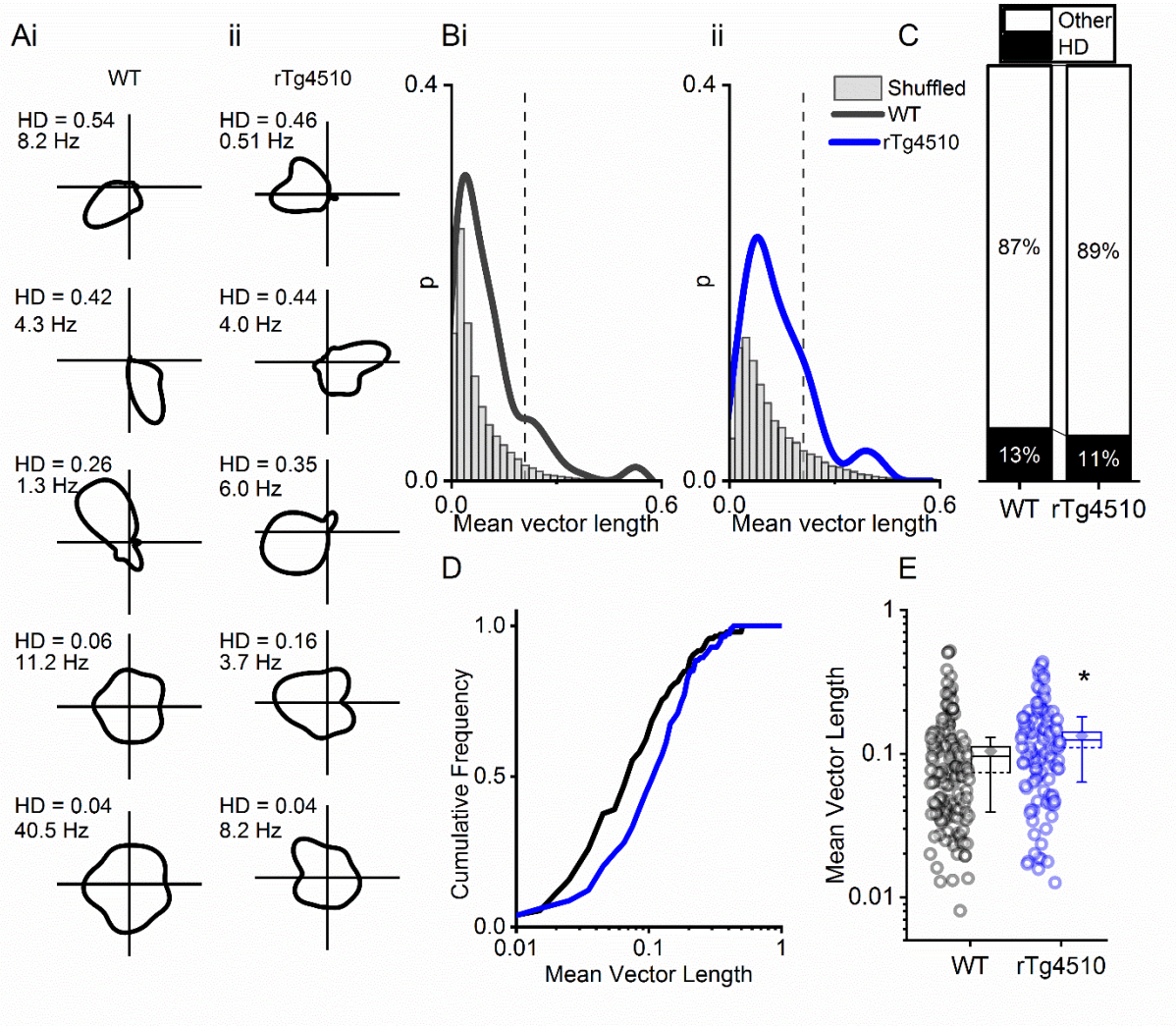

Figure 4: rTg4510 mice retain MEC head-direction tuning. A) Example head-direction tuning of 5 WT and 5 rTg450 units, displayed with head direction score (HD) and peak firing rate across head direction bins. **B)** Distribution of HD scores for WT (**i**) and rTg4510 mice (**ii**) with shuffled distribution of scores (grey), 95th-centile threshold: dotted line. **C)** Proportions of cells with head direction scores over threshold in WT and rTg4510 mice. **D)** Cumulative frequency distribution of HD scores (mean vector length). **E)** Mean vector length for all cells, showing a small but significant increase in head-direction tuning across the population in rTg410 mice (dotted line: median, diamond: mean ± SEM, whiskers: 25th/75th centile), * p<0.05 Mann-Whitney U test.

235

Discussion

Continuous integration of running speed information in the MEC has been proposed to be critically important for spatial navigation and path integration[5,8,31,45]. The current experiments clearly show that unlike WT animals, rTg4510 mice do not express adequate representations of locomotor activity in the MEC local field potential (LFP), since theta and gamma oscillations display blunted, or absent, relationships with running speed.

There has been some suggestion in the literature that dementia pathology affects the firing pattern of grid cells in the MEC both in mice[29] and grid-like neural representations in humans[30]. To date, however, no studies have examined changes to speed- or head direction-modulated firing of MEC single units in tauopathy. Our data suggest the hypothesis that reduced grid cell periodicity may be the result of the impaired integration of running speed information in the MEC.

Vulnerability of grid cell firing

These results highlight the importance of an intact path integration system in maintaining grid cell periodicity. Several studies have shown a breakdown of grid cell firing patterns after the inactivation of important spatial information streams. For example, inhibition of the medial septum, which controls theta rhythmicity, but also speed modulated inputs, produces a complete breakdown of grid cell periodicity[46,47]. Likewise, inactivation of the anterior thalamic nuclei (ATN) disrupts head direction tuning in the MEC, also impairing the grid cell signal[48]. Inactivation of reciprocal hippocampal inputs into the MEC is also sufficient to produce a breakdown in grid cell periodicity[49].

The almost complete breakdown of grid cell firing in rTg4510 mice contrasts with the effect on spatial representation in the hippocampus of these animals. While several studies have shown a reduction in the spatial information and stability of hippocampal place cells[19,26], firing fields are still consistently present in these mice. Given the pattern of degeneration across the hippocampal formation[39,50–52], poor place representation[19,26] may be the result of weakened entorhinal inputs[53–55]. Since hippocampal place cells could be thought of as conjunctive integrators of multiple spatial (and non-spatial) input streams, surviving inputs may facilitate encoding of an impoverished spatial representation in these mice[19,26]. However, the loss of grid/speed input prevents this from being anchored to an egocentric spatial reference frame, resulting decreased spatial stability. Presumably, whatever representation is being encoded by place cells is anchored to an allocentric reference frame. Decreasing the availability of visual/contextual cues or implementing a pure path integration task would likely exacerbate spatial learning/memory impairments. Reductions in grid and place field activity may therefore mirror their appearance in neuronal development, where place cells appear before grid cells but mature fully only after grid cell development[56,57]. The precise temporal nature of grid and place cell impairment in this model is as yet unknown. However, taken together, these data further suggest that hippocampal neurons can form place fields in the absence of effective grid cell firing.

Grid cells are proposed to play a key role in path integration[31,32,58,59]. For example, mice lacking GluA1-containing AMPA receptors have been shown to display reduced grid cell periodicity, correlating with impairments on a path integration-based task[60]. Path integration has also been suggested to be impaired in populations of dementia and MCI patients[13,15,17]. The direct association between these two factors is still unclear; however, it is likely that grid cell deficits, as described above, directly contribute to the deficits in memory in rTg4510 mice[19,50].

Negative speed modulation of MEC neurons

In WT animals, only a small population of MEC neurons display negative relationships with running speed[8,9]. These data show that during recordings on the linear track, rT4510 mice have a larger proportion of cells that decrease their firing rate with increases in running speed. Interestingly, neurons in the medial septum also display a more even split between positive and negative speed modulation[61], suggesting that, under normal physiological conditions, the MEC does not simply recapitulate these firing patterns, but integrates this information differently. The precise targets of negatively speed modulated inputs into MEC are unclear; however it is possible that they are more likely to be conjunctive with other spatial information systems, such as grid encoding or head direction. Indeed, negatively speed modulated cells are more likely to be tuned to head direction[9], which is consistent with the observed increase in mean vector length observed in rTg4510 neurons at a population level (Figure 4).

Stability of head direction tuning

A further feature of the inactivation studies described above[46–49] is the stability of head direction tuning in the MEC. Blocking medial septum activity impairs grid cell firing, but not head direction tuning[46,47]. Interestingly, the breakdown of grid periodicity after hippocampal inactivation has also been shown to reveal head direction tuning in grid cells that would previously not have been modulated by head direction[49]. It is possible that the small but significant population increase in head direction tuning in rTg4510 mice may reflect this unmasking of head direction inputs from cells that would have previously displayed grid patterns. However, this is a hypothesis that would need to be addressed directly with long term recordings of grid cells as tau pathology increased to critical levels to impair spatial firing patterns. This approach is unlikely to be achieved with current technology. In any case, the arrival of head direction information into the MEC is likely the result of an anatomically distinct pathway[62] that appears to be relatively preserved in the face of the tau pathology burden in

312 rTg4510 mice at this stage. This is most likely due to a greater dependence on subcortical
313 structures, such as the ATN, that integrate vestibular information[63–65].

314

315 *Impaired running speed representations in rTg4510 mice*

316 Theta oscillations show increases in both amplitude and frequency depending on running
317 speed (Figure 1). Spatially modulated MEC neurons are required to integrate large quantities
318 of multimodal sensory information from their environment. At fast running speeds, the time
319 window for this integration is smaller and it may therefore be necessary to increase the
320 sensitivity of such neurons during locomotion to accurately retrieve spatial associations from
321 memory. In rTg4510 mice, theta oscillation power appears to be independent of running speed
322 meaning that these animals are unable to integrate this information effectively.

323

324 In WT mice, the gamma oscillation power relationship with running speed shows a strong
325 predominance for fast gamma frequencies (Figure 1). This is consistent with the proposed
326 information flow across the hippocampal formation, in which the MEC provides the input
327 responsible for fast gamma frequencies in CA1 region of the hippocampus[66]. While the CA1
328 area has been shown to display two distinct peaks in the gamma band power spectra, MEC
329 LFP predominantly contains faster gamma frequencies only[66,67]. It is perhaps not surprising
330 then, that differences between genotypes (Figure 1) are only observed at these faster
331 frequencies. For this reason also, conclusions regarding the slow gamma oscillation frequency
332 should be made with caution. While slow gamma frequency has previously be shown to
333 display a negative speed relationship in the hippocampus, MEC correlations are generally
334 thought to be positive[36,68].

335 It is also worth noting that rTg4510 mice, like several other models of dementia, exhibit a
336 hyperactive phenotype[52,69–71], and hence altered patterns of locomotor activity. This may
337 reflect dysregulation of the septohippocampal pathway, activation of which has been shown

to stimulate movement or alternatively may reflect dysfunction in motor-related brain regions. Nevertheless, whilst it should be noted that rTg4510 mice are experiencing their environment at a generally higher state of arousal, at least in terms of locomotor activity, the key finding of this study is that this locomotor activity is improperly represented in the hippocampal formation.

Conclusions

Overall, these data show a clear breakdown in grid cell periodicity in rTg4510 mice compared to WT controls. In addition, they suggest a role for the dysfunctional processing of locomotor activity in this process, since the representation of running speed information in MEC single units is severely disrupted in these mice, while head direction tuning remains constant, or slightly increased. The changes to MEC single unit firing are likely to have profound implications for the impairments in spatial memory observed in these mice and suggest observable parameters to assess in dementia patient populations, for example through speed modulated fMRI signals in virtual environments.

Methods

Animals

All procedures were carried out in accordance with the UK Animal (Scientific Procedures) Act 1986 and were approved by the Universities of Exeter and Bristol Animal Welfare and Ethical Review Body.

Surgical implantation

All surgical procedures were conducted using standard sterile and aseptic techniques. Animals were anaesthetized using isoflurane (4%) and fixed into a stereotaxic frame (ASI instruments). Anaesthesia was reduced and maintained at 1-2% during surgery. After careful cleaning of the skull surface, small screws (Antrin Miniature Specialities) were inserted into each bone plate in order to anchor the electrode array. Silver wire (World Precision Instruments) was soldered to a screw overlying the cerebellum to be used as a ground.

Probes were implanted at 0.2-0.3 mm anterior to the transverse sinus and 3-3.25 mm from midline. Linear probes were implanted and fixed 3 mm below the dura mater and angled at 10 degrees in the posterior to anterior direction in the sagittal plane in order to record consistently from layer II/III along the dorsal-ventral axis of the MEC. High density 16- (Neuronexus) or dual shank 32-channel (Cambridge Neurotech) silicone probes were implanted 0.3-0.5 mm below dura at an angle of 5 degrees, also in the posterior direction and subsequently moved slowly into the cortex using their attached microdrive (Cambridge NeuroTech). RelyX Unicem 2 dental cement with blue curing light (Henry Schein) were used to anchor the probe to the skull and anchor screws.

376 *Data acquisition*

377 Animals were given at least 1 week of post-operative recovery before initial recording
378 sessions. Local field potential (LFP) signals were recorded using a Digital Lynx 10S recording
379 system (Neuralynx, Bozeman, MT, USA) tethered to a HS-18 or HS-36 unity gain headstage
380 and Cheetah 5 data acquisition software (Neuralynx). The headstage and tether were
381 counterbalanced using a moveable, weighted arm to allow for the maximum flexibility of
382 movement. Two light-emitting diodes (LEDs) on the headstage and an overhead video camera
383 (sample rate 25 Hz) were used to continuously track the animals' location using Cheetah's
384 built in video tracking software (VTS), allowing estimation of position and therefore running
385 speed. Once recorded, invalid tracking points, i.e. time-points where no light threshold was
386 reached, were excluded and the animal's position interpolated from the two nearest points.
387 Estimation of running speed was performed on binned position data, with erroneous bins,
388 above 50 cm/s, also removed. LFP data were recorded while animals explored either a linear
389 track (1.5 m) or square open field (0.8 m x 0.8 m).

390

391 *Analysis of local field potential (LFP) signal*

392 Data were continuously sampled at 2 kHz, band-pass filtered (1 – 500 Hz) and stored on a PC
393 for offline analysis. All LFP signals were analysed in MATLAB, using open-source toolboxes
394 or custom routines utilising built-in functions. Multi-tapered spectral analysis was performed
395 using the Chronux toolbox (available at http://chronux.org/).

396

397 Power and peak frequency of LFP frequency bands were compared to running speed. Spectral
398 analysis was conducted on 0.5 s bins of LFP data and compared to running speed calculated
399 from the same time frame. For running speed curves, locomotor activity was divided into 1
400 cm/s bins (between 1-30 cm/s) and oscillatory power and peak frequency averaged across all

relevant sections of data. Theta and gamma oscillation power was normalised to the power in these frequency bands during non-movement, defined as speeds under 1 cm/s.

Analysis of single unit data

For single unit data, recordings were referenced to the ground electrode, continuously sampled at 40 kHz, bandpass filtered between 1-30 kHz and saved unprocessed on a PC for offline analysis. Each channel was referenced offline to a common-average of the opposite 16-channel shank (250 µm away) in order to eliminate signals common across the electrode array such as noise and movement artefacts. Extracellular spike activity was detected and sorted using the klusta open source software package found at: http://klusta.readthedocs.io/en/latest/[72]. Clusters were classified as either putative interneurons or putative excitatory cells (pyramidal or stellate cells) by their spike half-width, taken from the peak to the subsequent trough of the average extracellular waveform. While the majority of cells recorded in the MEC are excitatory, a significant population can be classified as inhibitory interneurons[41,73,74]. Using the average spike waveform, putative interneurons were classified as displaying a spike-width less than 0.35 ms, based on the extracellular properties of PV+ interneurons isolated optogenetically[41]. This approach was taken alone, rather than in combination with average firing rare of neurons, since MEC interneurons have been shown to vary widely in their spike frequency[41]. Neurons were described by a theta modulation index (TMI), based on the fast Fourier transform (FFT) of spike-train autocorrelations, using methods described previously[19,40,75]. Autocorrelations were produced with ± 500 ms lags and 2 ms bin size. The peak at 0 lag was reduced to the next maximal value and the entire function mean-normalised by subtracting the mean from all values. The autocorrelation was tapered using a Hamming window to reduce spectral leakage and FFT calculated. The power spectrum was calculated by dividing the square of the FFT by the transform length (2^{16}, scaled to the length of the autocorrelation). TMI was defined as the mean power within 1 Hz of each side of the peak in the theta frequency range (5-12 Hz) dived

by the mean power between 0 and 125 Hz. Cells were defined as 'theta modulated' if their TMI was greater than 5.

Analysis of speed modulated firing

Speed modulation of single unit activity was calculated based on analysis described in Kropff *et al.*, (2015). Running speed and firing rate of individual clusters were calculated for 40 ms bins of data and smoothed across 500 ms using a Gaussian window function. Running speeds from 2-30 cm/s and containing more than 0.5% of total recording duration were used for further analysis. Speed modulation of cells was then defined by the correlation between all running speed and firing rate bins and a speed score calculated using the Fisher-z transformation of the correlation coefficient, r. Observed speed correlations were compared to a distribution of randomly sampled correlations of shuffled data. For shuffling, time stamps were forward-shifted by a pseudorandom period between 20 s and the total trial length minus 20 s, with the end of the trial wrapped to the beginning and reanalysed using the method above. Cells were defined as 'speed modulated' if their speed score (z) was greater than the 95th percentile, or less than the 5th percentile, of the global distribution of scores produced from at least 250 shuffled data sets for each unit (Figure 3).

Analysis of head direction properties

Head direction was determined by calculating the angle between two LEDs attached to the animal's headstage. Time periods where neither, or only one, of the LEDs were observed above threshold were discarded. Firing rate was calculated for 3º bins of head direction and smoothed, using a Gaussian window over 14º. A 'head direction score' was defined as the resultant mean vector length, calculated from the smoothed firing rate maps. Observed mean vector length was also compared to the 95th percentile of a distribution of shuffled data produced as above.

454 *Analysis of spatial firing properties*

455 Spike locations for each cell were obtained with a 2D histogram count, using the MATLAB
456 function *histcounts2*. Firing rate was calculated for 3 x 3 cm bins across recording
457 environments and smoothed using a 2D Gaussian function across 1.5 standard deviations.
458 'Gridness' was calculated using a 2D autocorrelation of smoothed firing rate maps[5]. Spatial
459 periodicity was determined by rotating autocorrelations in steps of 30°, between the central
460 peak and the 6 closest peaks, and correlating the rotated versions with the original. Grid score
461 was expressed as the difference between rotations at 30°, 90° and 150°, where if firing maps
462 show a hexagonal pattern give low correlations, and 60° and 120° where correlations will be
463 high.

464 The spatial information content (SI) of each cell was defined using the measure described by
465 Skaggs *et al.*, (1993) and expressed in terms of bits/spike. This approach measures the extent
466 to which a cell's firing rate can be used to predict the animal's location. By definition, this does
467 not assume spatial periodicity and has been used for quantifying place cell activity[19,27,55,76] as
468 well as spatially selective firing in the lateral EC[77].

469

470 *Hippocampal CA1 data*

471 Single unit and LFP data recorded from the CA1 pyramidal cell layer from previously published
472 datasets were additionally analysed for speed encoding (Booth *et al.*, (2016*b*)). These data
473 were collected using microdrives containing independently adjustable tetrodes, while animals
474 ran on a linear track. Running speed – firing rate relationships were determined using the
475 processing pathway described above.

476 *Electrode placement*

477 At the end of experiments, mice received a lethal overdose of sodium pentobarbital (Euthetal)
478 and electrolytic lesions were made at several electrode locations across the recording array.
479 Mice were then transcardially perfused with 4% v/v formaldehyde in 0.1 M phosphate buffered
480 saline (PBS). Brains were extracted from the skull and stored in 4% formaldehyde before being
481 cut in sagittal sections (50 µm) using a vibratome (Leica VT1000) and stained with cresyl
482 violet. The position of electrode sites was determined from digital pictures taken with a 2.5X
483 objective on a light microscope using QCapture pro 7 software (Qimaging). Probe electrode
484 location was expressed as distance from the most dorsal electrode site in layer II/III MEC.

485

Acknowledgments

This work was supported by an Alzheimer's Research UK Major Project Grant awarded to J.B. (ARUK-PG2017B-7). J.W. was an Alzheimer's Research UK Fellow (ARUK-RF2015-6). A.R. was a Royal Society Industry Fellow. K.P. is an employee of Eli Lilly and Company. Eli Lilly provided all the mice used in this study.

Author Contributions

Conceptualization, J.B., A.R., T.R; Methodology, K.P., T.R., J.W.; Investigation, T.R and J.W.; Writing – Original Draft, T.R. and JB.; Writing –Review & Editing, J.W., K.P., A.R., T.R. and J.B.; Funding Acquisition, J.B., J.W., A.R.; Resources, J.B., A.R., K.P.; Supervision, J.B., A.R.

Declaration of Interests

The authors declare no competing interests.

References

1. O'Keefe, J. & Dostrovsky, J. The hippocampus as a spatial map. Preliminary evidence from unit activity in the freely-moving rat. *Brain Res.* **34,** 171–175 (1971).
2. Fyhn, M., Molden, S., Witter, M. P., Moser, E. I. & Moser, M.-B. Spatial representation in the entorhinal cortex. *Science* **305,** 1258–64 (2004).
3. Hafting, T., Fyhn, M., Molden, S., Moser, M.-B. B. & Moser, E. I. Microstructure of a spatial map in the entorhinal cortex. *Nature* **436,** 801–6 (2005).
4. Giocomo, L. M. *et al.* Topography of head direction cells in medial entorhinal cortex. *Curr. Biol.* **24,** 252–62 (2014).
5. Sargolini, F. *et al.* Conjunctive representation of position, direction, and velocity in entorhinal cortex. *Science* **312,** 758–62 (2006).
6. Ranck, J. . Head-direction cells in the deep cell layers of dorsal presubiculum in freely moving rats. in *Society for Neuroscience Abstracts* **10,** (1984).
7. Valerio, S. & Taube, J. S. Path integration: how the head direction signal maintains and corrects spatial orientation. *Nat. Neurosci.* **15,** 1445–53 (2012).
8. Kropff, E., Carmichael, J. E., Moser, M.-B. & Moser, E. I. Speed cells in the medial entorhinal cortex. *Nature* **523,** 419–424 (2015).
9. Hinman, J. R., Brandon, M. P., Climer, J. R., Chapman, G. W. & Hasselmo, M. E. Multiple Running Speed Signals in Medial Entorhinal Cortex. *Neuron* **91,** 666–679 (2016).
10. Lever, C., Burton, S., Jeewajee, A., O'Keefe, J. & Burgess, N. Boundary vector cells in the subiculum of the hippocampal formation. *J. Neurosci.* **29,** 9771–7 (2009).
11. Solstad, T., Boccara, C. N., Kropff, E., Moser, M.-B. & Moser, E. I. Representation of geometric borders in the entorhinal cortex. *Science* **322,** 1865–8 (2008).
12. Barry, C. & Bush, D. From A to Z: a potential role for grid cells in spatial navigation. *Neural Syst. Circuits* **2,** 6 (2012).
13. Allison, S. L., Fagan, A. M., Morris, J. C. & Head, D. Spatial Navigation in Preclinical Alzheimer's Disease. *J. Alzheimer's Dis.* **52,** 77–90 (2016).
14. Lithfous, S., Dufour, A. & Després, O. Spatial navigation in normal aging and the prodromal stage of Alzheimer's disease: Insights from imaging and behavioral studies. *Ageing Res. Rev.* **12,** 201–213 (2013).
15. Hort, J. *et al.* Spatial navigation deficit in amnestic mild cognitive impairment. *Proc. Natl. Acad. Sci. U. S. A.* **104,** 4042–7 (2007).
16. Laczó, J. *et al.* Spatial navigation and APOE in amnestic mild cognitive impairment. *Neurodegener. Dis.* **8,** 169–77 (2011).
17. Mokrisova, I. *et al.* Real-space path integration is impaired in Alzheimer's disease and mild cognitive impairment. *Behav. Brain Res.* **307,** 150–158 (2016).
18. Pooler, A. M. *et al.* Propagation of tau pathology in Alzheimer's disease: identification of novel therapeutic targets. *Alzheimers. Res. Ther.* **5,** 49 (2013).
19. Booth, C. A. *et al.* Altered Intrinsic Pyramidal Neuron Properties and Pathway-Specific Synaptic Dysfunction Underlie Aberrant Hippocampal Network Function in a Mouse

Model of Tauopathy. *J. Neurosci.* **36,** 350–63 (2016).

20. Tamagnini, F. *et al.* Hippocampal neurophysiology is modified by a disease-associated C-terminal fragment of tau protein. *Neurobiol. Aging* **60,** 44–56 (2017).

21. Brown, J. T., Chin, J., Leiser, S. C., Pangalos, M. N. & Randall, A. D. Altered intrinsic neuronal excitability and reduced Na(+) currents in a mouse model of Alzheimer's disease. *Neurobiol. Aging* **32,** 2109.e1-e2109.e14 (2011).

22. Kerrigan, T. L., Brown, J. T. & Randall, A. D. Characterization of altered intrinsic excitability in hippocampal CA1 pyramidal cells of the Aβ-overproducing PDAPP mouse. *Neuropharmacology* **79,** 515–524 (2014).

23. Hoover, B. R. *et al.* Tau Mislocalization to Dendritic Spines Mediates Synaptic Dysfunction Independently of Neurodegeneration. *Neuron* **68,** 1067–1081 (2010).

24. Brown, J. T., Richardson, J. C., Collingridge, G. L., Randall, A. D. & Davies, C. H. Synaptic transmission and synchronous activity is disrupted in hippocampal slices taken from aged TAS10 mice. *Hippocampus* **15,** 110–117 (2005).

25. Fitzjohn, S. M. *et al.* Age-related impairment of synaptic transmission but normal long-term potentiation in transgenic mice that overexpress the human APP695SWE mutant form of amyloid precursor protein. *J. Neurosci.* **21,** 4691–8 (2001).

26. Cheng, J. & Ji, D. Rigid firing sequences undermine spatial memory codes in a neurodegenerative mouse model. *Elife* **2,** e00647 (2013).

27. Cacucci, F., Yi, M., Wills, T. J., Chapman, P. & O'Keefe, J. Place cell firing correlates with memory deficits and amyloid plaque burden in Tg2576 Alzheimer mouse model. *Proc. Natl. Acad. Sci.* **105,** 7863–7868 (2008).

28. Booth, C. A. *et al.* Electrical and Network Neuronal Properties Are Preferentially Disrupted in Dorsal, But Not Ventral, Medial Entorhinal Cortex in a Mouse Model of Tauopathy. *J. Neurosci.* **36,** 312–324 (2016).

29. Fu, H. *et al.* Tau Pathology Induces Excitatory Neuron Loss, Grid Cell Dysfunction, and Spatial Memory Deficits Reminiscent of Early Alzheimer's Disease. *Neuron* **93,** 533–541.e5 (2017).

30. Kunz, L. *et al.* Reduced grid-cell–like representations in adults at genetic risk for Alzheimer's disease. *Science (80-.).* **350,** (2015).

31. McNaughton, B. L., Battaglia, F. P., Jensen, O., Moser, E. I. & Moser, M.-B. B. Path integration and the neural basis of the 'cognitive map'. *Nat. Rev. Neurosci.* **7,** 663–78 (2006).

32. Burak, Y., Fiete, I. R., Trappenberg, T., Araujo, I. de & Wiggins, C. Accurate Path Integration in Continuous Attractor Network Models of Grid Cells. *PLoS Comput. Biol.* **5,** e1000291 (2009).

33. Bush, D. & Burgess, N. A hybrid oscillatory interference/continuous attractor network model of grid cell firing. *J. Neurosci.* **34,** 5065–79 (2014).

34. Ahmed, O. J. & Mehta, M. R. Running Speed Alters the Frequency of Hippocampal Gamma Oscillations. *J. Neurosci.* **32,** (2012).

35. McFarland, W. L., Teitelbaum, H. & Hedges, E. K. Relationship between hippocampal theta activity and running speed in the rat. *J. Comp. Physiol. Psychol.* **88,** 324–8 (1975).

36. Zheng, C., Bieri, K. W., Trettel, S. G. & Colgin, L. L. The relationship between gamma

584 frequency and running speed differs for slow and fast gamma rhythms in freely
585 behaving rats. *Hippocampus* **25,** 924–38 (2015).

586 37. Chen, Z., Resnik, E., McFarland, J. M., Sakmann, B. & Mehta, M. R. Speed controls
587 the amplitude and timing of the hippocampal gamma rhythm. *PLoS One* **6,** e21408
588 (2011).

589 38. Sławińska, U. & Kasicki, S. The frequency of rat's hippocampal theta rhythm is related
590 to the speed of locomotion. *Brain Res.* **796,** 327–331 (1998).

591 39. Ramsden, M. *et al.* Age-dependent neurofibrillary tangle formation, neuron loss, and
592 memory impairment in a mouse model of human tauopathy (P301L). *J. Neurosci.* **25,**
593 10637–47 (2005).

594 40. Langston, R. F. *et al.* Development of the Spatial Representation System in the Rat.
595 *Science (80-.).* **328,** (2010).

596 41. Buetfering, C., Allen, K. & Monyer, H. Parvalbumin interneurons provide grid cell–
597 driven recurrent inhibition in the medial entorhinal cortex. *Nat. Neurosci.* **17,** 710–8
598 (2014).

599 42. Skaggs, W. E., Mcnaughton, B. L., Gothard, K. M. & Markus, E. J. An Information-
600 Theoretic Approach to Deciphering the Hippocampal Code. *Neural Inf. Process. Syst.*
601 1030–1037 (1993).

602 43. McNaughton, B. L., Barnes, C. A. & O'Keefe, J. The contributions of position,
603 direction, and velocity to single unit activity in the hippocampus of freely-moving rats.
604 *Exp. Brain Res.* **52,** 41–49 (1983).

605 44. Lu, X. & Bilkey, D. K. The velocity-related firing property of hippocampal place cells is
606 dependent on self-movement. *Hippocampus* **20,** NA-NA (2009).

607 45. Burgess, N., Barry, C. & O'Keefe, J. An oscillatory interference model of grid cell
608 firing. *Hippocampus* **17,** 801–12 (2007).

609 46. Brandon, M. P. *et al.* Reduction of theta rhythm dissociates grid cell spatial periodicity
610 from directional tuning. *Science* **332,** 595–9 (2011).

611 47. Koenig, J., Linder, A. N., Leutgeb, J. K. & Leutgeb, S. The Spatial Periodicity of Grid
612 Cells Is Not Sustained During Reduced Theta Oscillations. *Science (80-.).* **332,**
613 (2011).

614 48. Winter, S. S., Clark, B. J. & Taube, J. S. Disruption of the head direction cell network
615 impairs the parahippocampal grid cell signal. *Science (80-.).* **347,** (2015).

616 49. Bonnevie, T. *et al.* Grid cells require excitatory drive from the hippocampus. *Nat.*
617 *Neurosci.* **16,** 309–317 (2013).

618 50. Santacruz, K. *et al.* Tau suppression in a neurodegenerative mouse model improves
619 memory function. *Science* **309,** 476–81 (2005).

620 51. Spires, T. L. *et al.* Region-specific dissociation of neuronal loss and neurofibrillary
621 pathology in a mouse model of tauopathy. *Am. J. Pathol.* **168,** 1598–607 (2006).

622 52. Blackmore, T. *et al.* Tracking progressive pathological and functional decline in the
623 rTg4510 mouse model of tauopathy. *Alzheimers. Res. Ther.* **9,** 77 (2017).

624 53. Hales, J. B. *et al.* Medial Entorhinal Cortex Lesions Only Partially Disrupt
625 Hippocampal Place Cells and Hippocampus-Dependent Place Memory. *Cell Rep.* **9,**
626 893–901 (2014).

54. Van Cauter, T., Poucet, B. & Save, E. Unstable CA1 place cell representation in rats with entorhinal cortex lesions. *Eur. J. Neurosci.* **27,** 1933–46 (2008).

55. Brun, V. H. *et al.* Impaired Spatial Representation in CA1 after Lesion of Direct Input from Entorhinal Cortex. *Neuron* **57,** 290–302 (2008).

56. Wills, T. J., Barry, C. & Cacucci, F. The abrupt development of adult-like grid cell firing in the medial entorhinal cortex. *Front. Neural Circuits* **6,** 21 (2012).

57. Muessig, L., Hauser, J., Wills, T. J. & Cacucci, F. A Developmental Switch in Place Cell Accuracy Coincides with Grid Cell Maturation. *Neuron* **86,** 1167–73 (2015).

58. Fuhs, M. C. & Touretzky, D. S. A Spin Glass Model of Path Integration in Rat Medial Entorhinal Cortex. *J. Neurosci.* **26,** (2006).

59. Etienne, A. S. & Jeffery, K. J. Path integration in mammals. *Hippocampus* **14,** 180–192 (2004).

60. Allen, K. *et al.* Impaired Path Integration and Grid Cell Spatial Periodicity in Mice Lacking GluA1-Containing AMPA Receptors. *J. Neurosci.* **34,** (2014).

61. Justus, D. *et al.* Glutamatergic synaptic integration of locomotion speed via septoentorhinal projections. *Nat. Neurosci.* **20,** 16–19 (2016).

62. Taube, J. S. The Head Direction Signal: Origins and Sensory-Motor Integration. *Annu. Rev. Neurosci.* **30,** 181–207 (2007).

63. Stackman, R. W. & Taube, J. S. Firing properties of rat lateral mammillary single units: head direction, head pitch, and angular head velocity. *J. Neurosci.* **18,** 9020–37 (1998).

64. Blair, H. T., Welday, A. C. & Zhang, K. Scale-invariant memory representations emerge from moiré interference between grid fields that produce theta oscillations: a computational model. *J. Neurosci.* **27,** 3211–29 (2007).

65. Sharp, P. E., Tinkelman, A. & Cho, J. Angular velocity and head direction signals recorded from the dorsal tegmental nucleus of gudden in the rat: Implications for path integration in the head direction cell circuit. *Behav. Neurosci.* **115,** 571–588 (2001).

66. Colgin, L. L. *et al.* Frequency of gamma oscillations routes flow of information in the hippocampus. *Nature* **462,** 353–7 (2009).

67. Chrobak, J. J. & Buzsaki, G. Gamma Oscillations in the Entorhinal Cortex of the Freely Behaving Rat. *J. Neurosci.* **18,** 388–398 (1998).

68. Kemere, C., Carr, M. F., Karlsson, M. P. & Frank, L. M. Rapid and continuous modulation of hippocampal network state during exploration of new places. *PLoS One* **8,** e73114 (2013).

69. Jul, P. *et al.* Hyperactivity with Agitative-Like Behavior in a Mouse Tauopathy Model. *J. Alzheimer's Dis.* **49,** 783–795 (2015).

70. Cheng, D., Low, J. K., Logge, W., Garner, B. & Karl, T. Novel behavioural characteristics of female APPSwe/PS1ΔE9 double transgenic mice. *Behav. Brain Res.* **260,** 111–118 (2014).

71. Przybyla, M. *et al.* Disinhibition-like behavior in a P301S mutant tau transgenic mouse model of frontotemporal dementia. *Neurosci. Lett.* **631,** 24–29 (2016).

72. Rossant, C. *et al.* Spike sorting for large, dense electrode arrays. *Nat. Neurosci.* **19,** 634–41 (2016).

670 73. Beed, P. *et al.* Inhibitory gradient along the dorsoventral axis in the medial entorhinal
671 cortex. *Neuron* **79,** 1197–207 (2013).

672 74. Miettinen, M., Koivisto, E., Riekkinen, P. & Miettinen, R. Coexistence of parvalbumin
673 and GABA in nonpyramidal neurons of the rat entorhinal cortex. *Brain Res.* **706,** 113–
674 122 (1996).

675 75. Wills, T. J., Cacucci, F., Burgess, N. & O'Keefe, J. Development of the hippocampal
676 cognitive map in preweanling rats. *Science* **328,** 1573–6 (2010).

677 76. Hussaini, S. A., Kempadoo, K. A., Thuault, S. J., Siegelbaum, S. A. & Kandel, E. R.
678 Increased size and stability of CA1 and CA3 place fields in HCN1 knockout mice.
679 *Neuron* **72,** 643–53 (2011).

680 77. Deshmukh, S. S. & Knierim, J. J. Representation of non-spatial and spatial
681 information in the lateral entorhinal cortex. *Front. Behav. Neurosci.* **5,** 69 (2011).

682

683 **Supplementary figures**

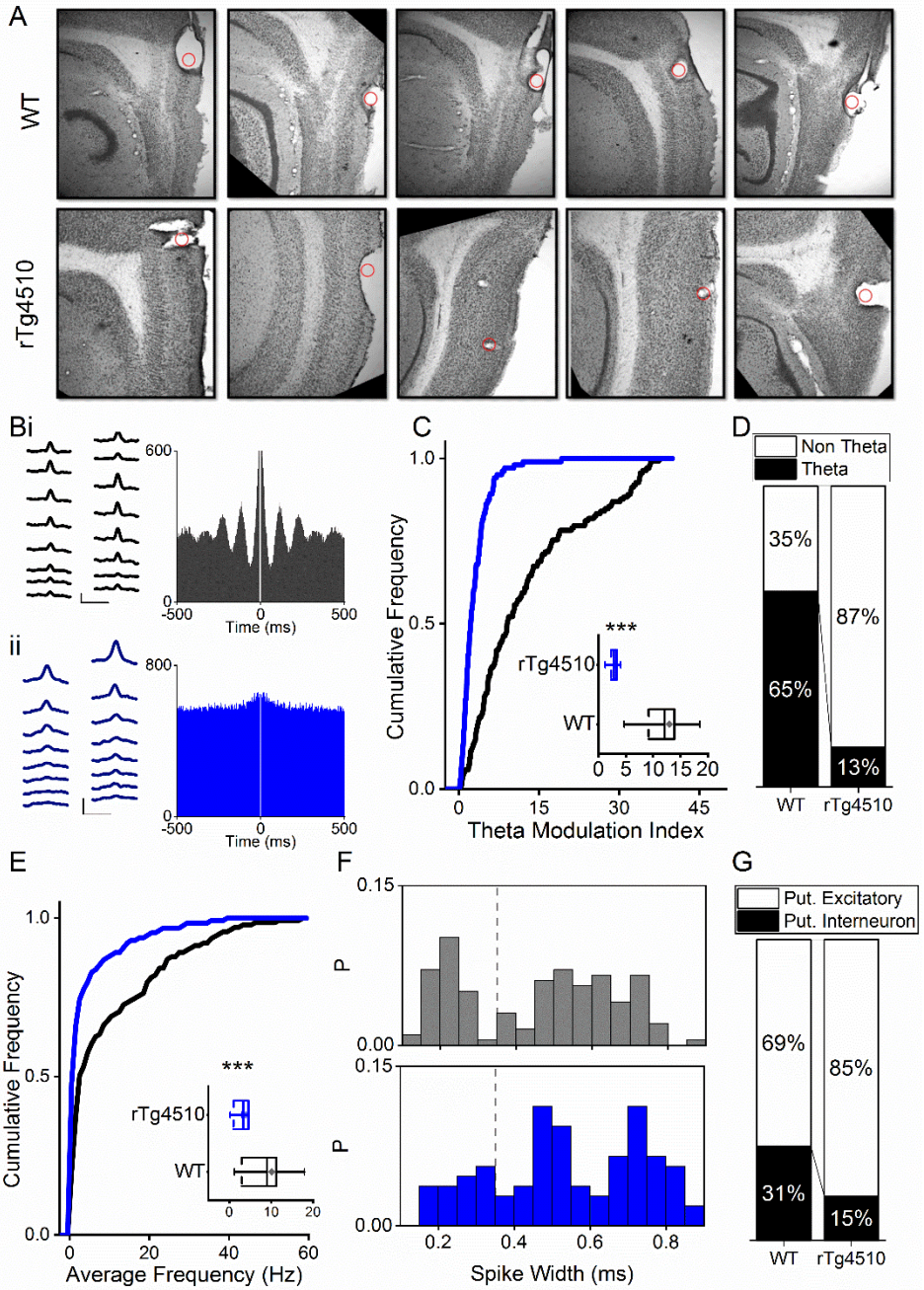

684

Figure S1: Firing properties of mEC single units. A) Example sections showing electrode lesions (red dot) of final probe location in mEC of WT and rTg4510 mice. **B)** Average waveforms from an example cell recorded from a 16 channel silicone probe shank for WT (**i**) and rTg4510 (**ii**) mouse, with firing autocorrelations. Scale bars: 0.4 ms, 50 µV. **C)** Cumulative frequency plot of theta modulation index for all recorded mEC single units, with average modulation for WT (black) and rTg4510 (blue) mice inset. **D)** Proportion of cells displaying theta modulation (threshold: TMI>5). **E)** Average firing frequency across entire recording session of mEC neurons for WT (black) and rTg4510 (blue) mice, average inset. **F)** Spike-width probability histogram for WT (black) and rTg4510 (blue) units. **G)** Proportion of cells classified as putative interneurons (spike-width <0.35 ms, dotted line in E) and putative excitatory. Box plots: dotted line: median, diamond: mean ± SEM, whiskers: 25th/75th centile), *** p <0.001 Mann-Whitney U test.

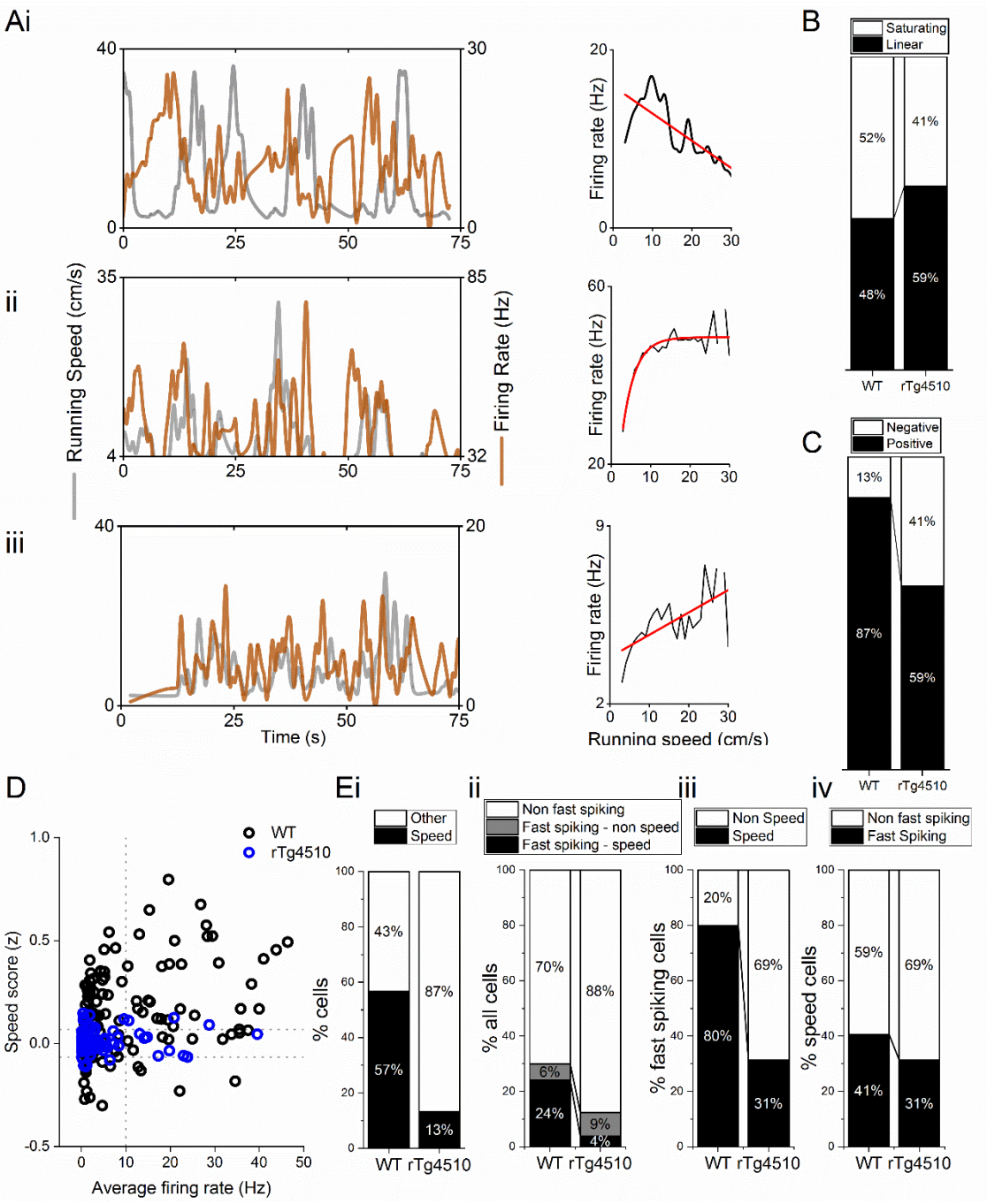

Figure S2: Properties of MEC speed modulated cells. A) Example negative (**i**), saturating **(ii)** and linear (**iii**) speed-modulated cells, with running speed (grey) and cell firing rate (orange), with average for each speed bin (1 cm/s) (right). Red line: linear/exponential fit for each. **B)** Proportion of speed modulated mEC cells that are best described by linear and saturating fits for WT and rTg4510 mice. **C**) Proportion of speed modulated units that show positive (>95th centile of shuffled distribution) and negative (<5th centile of shuffled distribution) speed modulation. **D)** Plot of speed score vs average firing rate, showing faster-spiking cells are more likely to have high speed modulation in WT, but not rTg4510 mice. **Ei)** Proportion of speed-modulated cells in WT and rTg4510 mice (replotted from Fig 3E). **ii)** Proportions of cells classified as fast-spiking (>10 Hz), with breakdown into speed and non-speed modulators for each genotype. **iii)** Proportion of fast spiking cells which display speed modulation, which shows decreased numbers in rTg4510 mice compared to WT. **iv)** Proportion of speed modulated cells which are classified as fast spiking shows only small decrease in rTg4510 mice.

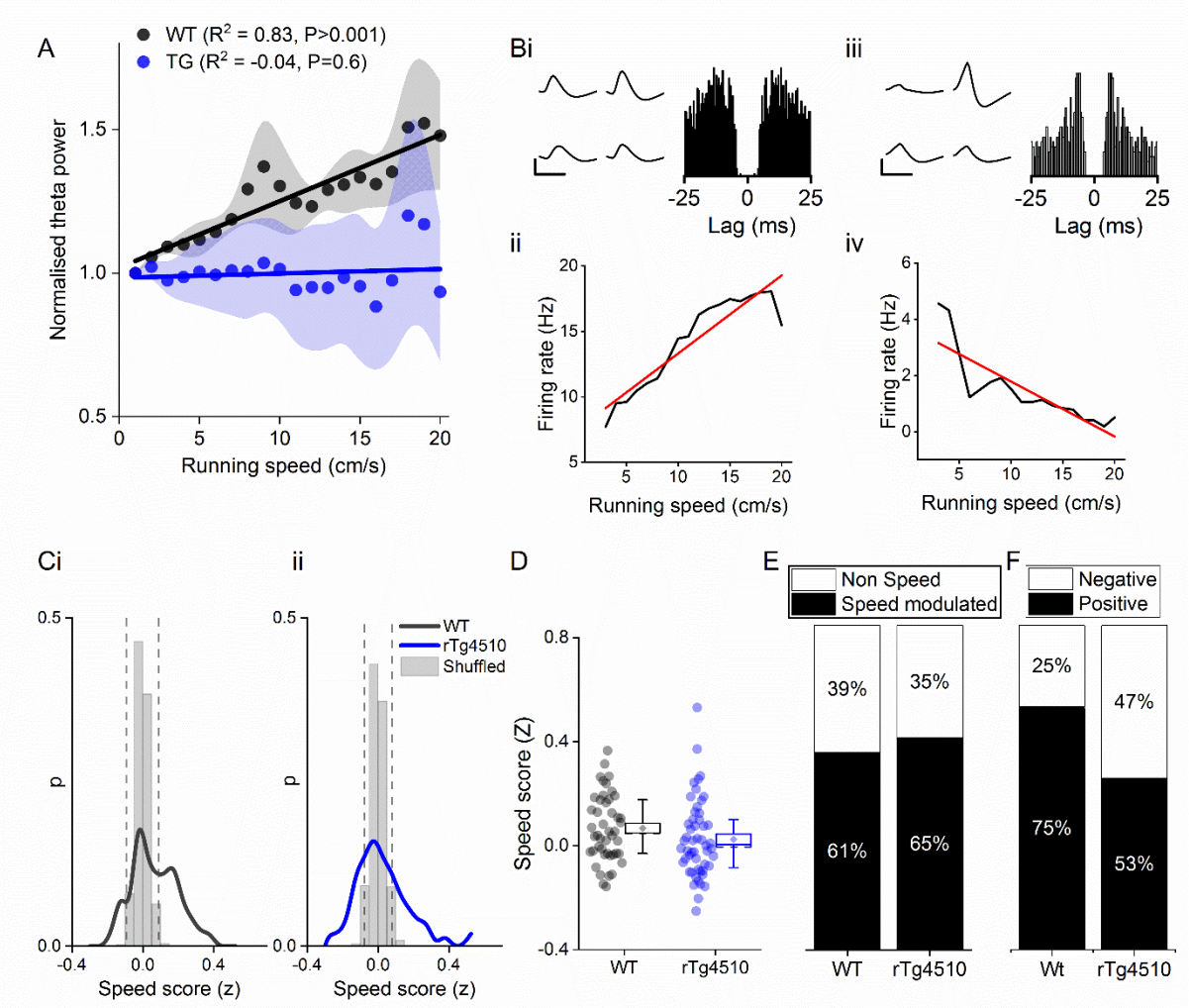

Figure S3: Speed modulation of single units in hippocampal CA1 pyramidal cell layer also shows similar increase in negatively speed modulated firing. A) Normalised theta oscillation amplitude from WT and rTg4510 mice with increasing running speed, with average linear regression above (WT: $R^2 = 0.83$, $p < 0.001$, n = 6 mice; rTg4510: $R^2 = -0.04$, $p = 0.6$, n = 4 mice). **B**) Example speed-modulated cells recorded from the CA1 pyramidal cell layer. The cell on the left (i and ii) was positively speed-modulated, whilst the cell on the right (iii and iv) was negatively speed-modulated. **C**) histograms of speed scores for WT and rTg4510 mice. 5^{th} and 95^{th} centiles of shuffled data shown as dotted lines. **D**) box plot comparing speed scores between the two genotypes **E)** Proportion of cells passed criteria for speed modulated firing is approximately even between genotypes (WT: 25/46 units, rTg4510: 27/52 units). **F)** Increased proportion of negatively speed modulated units in CA1 in rTg4510 mice, compared to WT controls (WT: 5/25 units, rTg4510:13/27 units; χ^2 (1) = 4.5, p = 0.03, Chi-Square test).

686

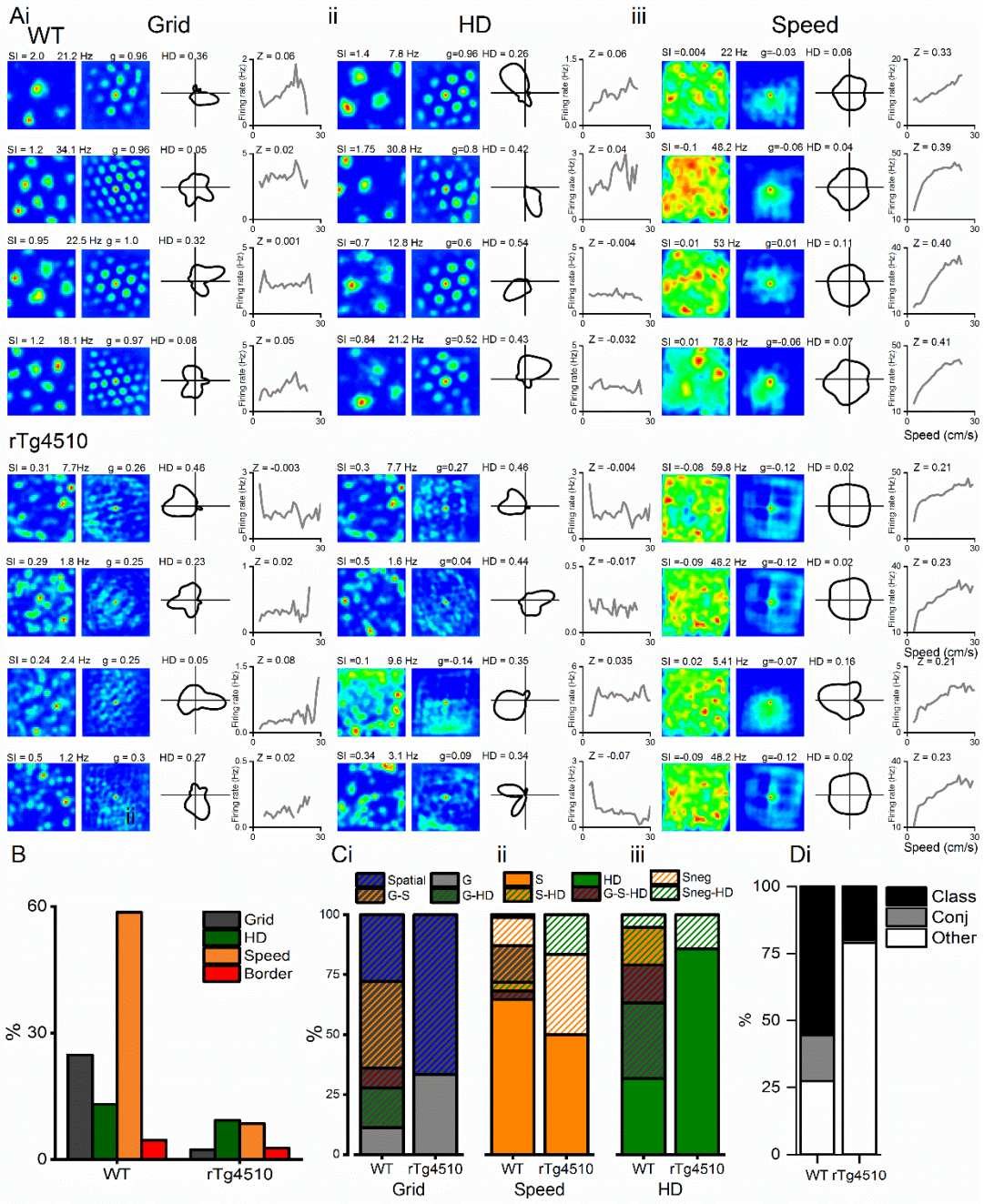

Figure S4: Conjunctive representation of grid, head direction and running speed in WT and rTg4510 mice. A) Example grid **(i)**, head direction **(ii)** and speed **(iii)** cells taken from the highest modulation scores from WT (top) and rTg4510 (bottom) mice, showing spatial firing patterns with 2D spatial autocorrelation, head direction tuning and running speed-firing rate relationship and corresponding score (SI: spatial information, HD: mean vector length, Z: speed score). **B)** Proportions of grid, head-direction and speed modulated cells recorded in mEC, showing reduced number of grid and speed, but not head-direction, cells passing threshold (95% centile of shuffled distribution). **C)** Conjunctive proportions of grid cells **(i)**, head direction cells **(ii)** and speed modulated cells **(iii)** recorded from WT and rTg4510 mice scaled to 100%. **D)** Breakdown of units from WT and rTg4510 mice that satisfied a single criteria (class), multiple criteria (conj) or no discernible firing pattern (other). Key, G: grid, S: speed, HD: head direction, G-S: grid-speed, G-HD: grid-head direction, G-S-HD: grid-speed-head direction, SnegHD: negative speed–head-direction, Sneg: negative speed, Class: classed as cell type, Conj: conjunctive representation (more than 1 classification), other: not classified as grid, speed or HD.

687